ELSEVIER

Dynamics of Atmospheres and Oceans
31 (2000) 209–232

dynamics of atmospheres and oceans

www.elsevier.com/locate/dynatmoce

Internal waves revisited

B.R. Sutherland *, G.O. Hughes [1], S.B. Dalziel, P.F. Linden [2]

Department of Applied Mathematics and Theoretical Physics, Silver Street, Cambridge CB3 9EW, UK

Received 25 June 1998; received in revised form 19 January 1999; accepted 23 March 1999

Abstract

We describe a new laboratory technique that has been developed to examine the structure and amplitude of internal waves. As well as being relatively inexpensive to set up, the technique is sensitive to small density fluctuations: heat rising from a hand can easily be seen. If the internal wave field is uniform across the span of the tank, then the density gradient field can be measured non-intrusively everywhere in space and time. We use this technique to measure the amplitude of internal waves generated by a circular cylinder that oscillates at an angle with the vertical, and we examine how the amplitude and phase of the waves changes as a function of the angle of oscillation. The experimental results are compared with analytic theory. Generally, the theory agrees well with experimental results although some consistent discrepancies exist which in part we attribute to the effects of a viscous boundary layer surrounding the cylinder.

Keywords: Internal waves; Density gradient field; Tank

1. Introduction

Internal waves propagate due to buoyancy restoring forces acting in a density stratified medium. Nastrom and Fritts (1992) have demonstrated by analysis of aircraft records of atmospheric turbulence that the most significant source of internal waves in

* Corresponding author. Department of Mathematical Sciences, University of Alberta, Edmonton, AB Canada, T6G 2G1. E-mail: bruce.sutherland@ualberta.ca; Web: http://taylor.math.ualberta.ca/ ~ bruce

[1] Present address: Research School of Earth Sciences, The Australian National University, Canberra, A.C.T. 0200, Australia.

[2] Present address: Department of Applied Mechanics and Engineering Science, University of California, San Diego, 9500 Gilman Drive, La Jolla, CA 92093-0411, USA.

0377-0265/00/$ - see front matter
PII: S0377-0265(99)00034-2

the atmosphere are in mountainous regions. The waves are generated by the flow of wind over mountains which force the stratified air upward and downward (e.g., see Lilly, 1971; Wurtele et al., 1996). Likewise, in the ocean, internal waves have been observed to be generated near the continental shelf edge (e.g., see Wunsch, 1975; Huthnance, 1989), over sills such as the Strait of Gibraltar (e.g., see Brandt et al., 1996), and by flow over deep ocean ridges (e.g., see Konyaev et al., 1995). The linear theory for internal waves generated by small amplitude forcing is well established for isolated (Long, 1955) and periodic (Gill, 1982, Section 6) topography. In numerical models of large-scale atmospheric and oceanic flows, linear theory is often employed to model the generation of internal waves. However, if the horizontal and vertical scales of the topography are comparable, the applicability of linear theory is drawn into question.

We have begun a program of research to evaluate the effectiveness of linear theory in predicting the structure and amplitude of internal waves generated by a localised source. We use a new experimental technique called ''synthetic schlieren'' that allows us for the first time to measure non-intrusively the amplitude of spanwise-uniform internal waves everywhere in space and time. If the waves are not spanwise-uniform, the technique nonetheless provides an average measure of their spanwise properties. In the work presented here, we examine the internal wave field produced by a circular cylinder oscillating at a range of angles to the vertical. Although not directly applicable to the study of mountain waves, this simple geometry provides an historically precedented starting point. We compare our results with classic experiments performed originally by Mowbray and Rarity (1967), and we compare the observed amplitude of the waves with the amplitude predicted theoretically by Hurley and Keady (1997). In particular, by determining where discrepancies occur between theory and the experimentally measured structure and amplitude of the waves as a function of the amplitude and angle of oscillation of the source, we are able to assess where models of the coupling between the fluid response and the source may be improved.

Mowbray and Rarity (1967) examined internal waves generated by a vertically oscillating circular cylinder in uniformly stratified fluid. Using a classical schlieren technique, they showed that internal waves generated by an oscillating cylinder emanate along four beams forming the pattern of a ''St. Andrew's Cross'' with the cylinder at the centre. Each beam is inclined at an angle Θ to the vertical, this angle being determined by the frequency, ω, of the oscillations and the background buoyancy frequency, $N(z)$. For a stratified Boussinesq fluid, the squared buoyancy frequency N^2 is given by

$$N^2(z) = -\frac{g}{\rho_0}\frac{\mathrm{d}\bar{\rho}}{\mathrm{d}z}, \tag{1}$$

in which g is the gravitational acceleration, ρ_0 is a reference value of density, and $\overline{\rho(z)}$ is the vertical profile of the background density as a function of height z. From the linear dispersion relation for internal waves (e.g., see Lighthill, 1978), it can be shown that if $\omega < N$, then

$$\Theta = \cos^{-1}(\omega/N). \tag{2}$$

A variety of studies have employed linear theory to predict the structure and amplitude of the internal wave-beams generated by an oscillating source. For a vibrating point source in inviscid fluid, Makarov et al. (1990) showed that wave motion is aligned along beams of infinitesimal width, the shear across the beam being infinite. In a theory including the effects of viscosity, this unphysical singularity does not occur. Viscosity acts to attenuate and broaden the beam with distance from the source. Thomas and Stevenson (1972) found a similarity solution for the beam attenuation, showing that the beam width increases as $r^{1/3}$ and the fluid displacement decreases as r^{-1} with distance r from the cylinder. These results were confirmed experimentally by Peters (1985). For a finite-sized source, the width of the beams has been found to be comparable with the source size (Appleby and Crighton, 1986, 1987; Voisin, 1991; Hurley and Keady, 1997), however, the qualitative structure of the beams varies depending on the ratio of the source size d compared with the viscous length scale

$$l_{\mathrm{v}} = \frac{(g\upsilon)^{1/3}}{N}, \tag{3}$$

where υ is the kinematic viscosity. If $l_{\mathrm{v}} \ll d$, then, the beams are bimodal; that is, they consist of two bands which emanate from the tangential extremities of the source (Kistovich et al., 1990; Makarov et al., 1990). If $l_{\mathrm{v}} \gg d$, then, the beams are unimodal: the maximum amplitude is along the centre of each beam. If the viscous length scale is relatively small so that the beams close to the cylinder are bimodal, then, Makarov et al. (1990) predicted that wave-beams would be attenuated by viscosity and have a unimodal structure for $r > R_{\mathrm{v}}$, where

$$R_{\mathrm{v}} = \frac{g}{N^2} R^3 / l_{\mathrm{v}}^3 = \frac{NR^3}{\upsilon}, \tag{4}$$

in which R is the radius of the cylinder. For large r/R, however, the assumptions used to derive Eq. (4) may not be valid, and it is possible for the transition from bimodal to unimodal wave-beam structures to occur over a much shorter distance than R_{v}. Indeed, in their experiments of a vertically oscillating cylinder, Sutherland et al. (1999) have shown that R_{v} significantly overestimates this transition distance.

Recently, analytic solutions have been derived from linear theory of internal waves generated by a cylinder that oscillates about a range of angles to the vertical in uniformly stratified, inviscid (Hurley, 1997) and viscous (Hurley and Keady, 1997) fluid. A summary of the latter is given in Section 2. This theory employs the ''boundary layer approximation'' of Thomas and Stevenson (1972), in which it is assumed that along-beam motions dominate over across-beam motions. Their solutions qualitatively reproduce the transition from near-cylinder bimodal to far field unimodal beams. However, the ''boundary layer approximation'' is inapplicable near the source where viscous boundary layers surround the cylinder. With the synthetic schlieren technique it is now possible to examine the range of accuracy of the theory when applied to finite-amplitude waves with a finite-sized boundary layer surrounding the cylinder. In experiments using the technique, we measure the amplitude and structure of the waves

generated by an oscillating cylinder, and we compare our results with theory to evaluate the effect of the boundary layer upon the far field evolution of the waves. This work, in particular, examines how the structure and amplitude of the waves change when a circular cylinder oscillates at different angles to the vertical.

In Section 3, we give a brief historical review of schlieren and interferometric techniques and we describe how synthetic schlieren may be used to measure quantitatively the amplitude of a spanwise uniform internal wave field everywhere in space and time. Section 4 describes the experimental results, and these are compared with theory in Section 5. A summary is given in Section 6.

2. Theory

Here, we review the linear theory of internal waves generated by an oscillating cylinder in viscous fluid, the analytic solutions for which have been found by Hurley and Keady (1997). We consider a cylinder oscillating with frequency ρ in a uniformly stratified fluid with buoyancy frequency N. The displacement of the cylinder in time t is given by $(A_x, A_z)\exp(-\iota\omega t)$, in which A_x is the horizontal and A_z the vertical component of the displacement vector. It is convenient to write the amplitude $(A_x, A_z) = A(-\sin\phi, \cos\phi)$, in which ϕ is the angle of oscillation measured anti-clockwise from the vertical as shown in Fig. 1. It is assumed that the resulting two-dimensional wave field is oscillatory with frequency ω and may be represented in terms of the streamfunction $\psi(x,z)\exp(-\iota\omega t)$. The Boussinesq approximation is employed and the

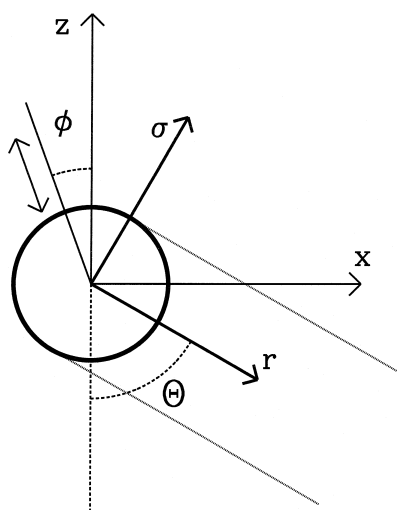

Fig. 1. A schematic showing the (σ, r) co-ordinate system for the down and rightward wave beam propagating at an angle Θ with the vertical.

waves are assumed to be of small amplitude so that linear theory applies. Under these assumptions, it can easily be shown that $\psi(x,z)$ satisfies

$$N^2\frac{\partial^2\psi}{\partial x^2} - \omega^2\nabla^2\psi + \iota\omega\nu\nabla^4\psi = 0. \tag{5}$$

The solution of this equation is found for ψ along the internal wave beam propagating downward and to the right of the cylinder. Eq. (5) is re-expressed in an orthogonal co-ordinate system with axes in the along-beam (r) and across-beam (σ) directions, as shown schematically in Fig. 1. The relationship between (r,σ) and (x,z) is given by

$$\sigma = x\cos\Theta + z\sin\Theta, \quad r = x\sin\Theta - z\cos\Theta, \tag{6}$$

in which Θ is the angle the r-axis makes with the vertical. In the (r,σ) co-ordinate system, Eq. (5) is further simplified by applying the ''boundary-layer approximation'' (Thomas and Stevenson, 1972) which assumes that gradients in the across-beam direction are much larger than those in the along-beam direction. Thus, we obtain

$$-\frac{\partial^2\psi}{\partial\sigma\partial r} + \frac{\iota\nu}{2\omega\tan\Theta}\frac{\partial^4\psi}{\partial\sigma^4} = 0. \tag{7}$$

The solution to Eq. (7) for the right and downward propagating wave beam is given by

$$\psi = \frac{AR\omega}{2}\mathrm{e}^{\iota(\Theta-\phi)}\int_0^\infty \frac{J_1(K)}{K}\exp\left(-K^3\lambda\frac{r}{R} + \iota K\frac{\sigma}{R}\right)\mathrm{d}K, \quad r>0, \tag{8}$$

in which $\lambda = \nu/2R^2\omega\tan\Theta$ and J_1 is the first order Bessel function of the first kind (Hurley and Keady, 1997). Effectively, ψ is determined from an integral over the non-dimensional across-beam wavenumber K.

For comparison with experiments, we wish to find the solution in terms of the change in the squared buoyancy frequency, which is related to the vertical gradient of the perturbation density field, $\rho(x,z)$, by $\Delta N^2 = -(g/\rho_0)\mathrm{d}\rho/\mathrm{d}z$. Using linear theory, we find that $\Delta N^2 = (-\iota/\omega)N^2(\partial^2\psi/\partial x\partial z)$. Hence,

$$\Delta N^2 = \frac{-\iota}{2}ARN^2\mathrm{e}^{\iota(\Theta-\phi)}\left[\int_0^\infty\left(-\frac{1}{2}(\lambda^2k^4R^4+1)k^2\sin2\Theta - \iota\lambda k^4R^2\cos2\Theta\right)\right.$$
$$\left.\times\frac{J_1(Rk)}{k}\exp(-R^2k^3\lambda r + \iota k\sigma)\mathrm{d}k\right], \tag{9}$$

where we have defined the dimensional across-beam wavenumber $k = K/R$ (Sutherland et al., 1999). For fixed values of r, this integral is solved using a discrete fast Fourier transform algorithm (Press et al., 1993, Section 12.2).

3. Experimental method

Synthetic schlieren is a new technique that is relatively inexpensive to set up, and which provides a robust method for visualising and measuring small amplitude, two-di-

mensional internal waves. Below, we briefly review other schlieren techniques, we describe the set-up for the experiments reported here, and we explain how the amplitude of internal waves is measured using synthetic schlieren. A detailed review of schlieren, interferometric and similar techniques and a more general discussion of synthetic schlieren is given by Dalziel et al. (1999) and Sutherland et al. (1999).

3.1. Review of schlieren techniques

Schlieren techniques (Toepler, 1864; Mowbray and Rarity, 1967; Thomas and Stevenson, 1972) have often been used to visualise the field of internal waves produced by an oscillating cylinder in salt-stratified water. The methods take advantage of the fact that the index of refraction n of salt water varies as a function of salinity, and that light rays passing through stratified fluid at angles close to the horizontal are deflected as they propagate through fluid of varying refractive index. The degree to which they are deflected depends upon the density gradient. An internal wave acts to stretch and compress isopycnal surfaces and thereby change the local density gradient. The path followed by light rays is thereby deflected to a greater or lesser degree.

In the classical schlieren technique, a light source reflects off a large parabolic mirror to create parallel beams of light that pass through a test section of the tank filed with salt-stratified water. A second parabolic mirror refocusses the beam, and a knife edge at the focus removes parts of the beam that are deflected from their parallel path when passing through the tank. The parabolic mirrors required to focus the beams are expensive, difficult to set up, and allow a relatively small field of view.

The Moiré fringe method (Sakai, 1990) operates in a similar manner to classical schlieren, but replaces the pair of parabolic mirrors and knife edge by a pair of accurately aligned masks. These masks consist of a set of parallel lines and are normally aligned so that 50% of the light passing through the first mask on one side of the test section is stopped by the second ‘‘analysing’’ mask on the other side of the test section. Due to camera parallax, the lines on the mask in front of the tank are more closely spaced than those to the rear of the tank. The Moiré fringe method is cheaper to implement and may be scaled up to cover larger domains more readily than classical schlieren. The main difficulty is that the alignment between the apparent position of the mask behind the tank and the analysing-mask in front of the tank is critical and non-trivial, especially if light entering the camera is not approximately parallel or if the stratification is non-uniform so that the line spacings are not related by a simple scale factor.

The synthetic schlieren method overcomes this difficulty by eliminating the need for the analysing-mask used in the Moiré fringe method. It does so by creating a ‘‘virtual’’ mask that is generated digitally. Thus, synthetic schlieren is not only more robust, but also capable of quantitatively measuring wave amplitudes. Details of how the method works and how quantitative measurements are made are given in Section 3.2.

3.2. Set-up of experiment and synthetic schlieren

Fig. 2 shows the typical set-up (not to scale) of an experiment using synthetic schlieren to visualise internal waves. Light rays, which emanate from an image

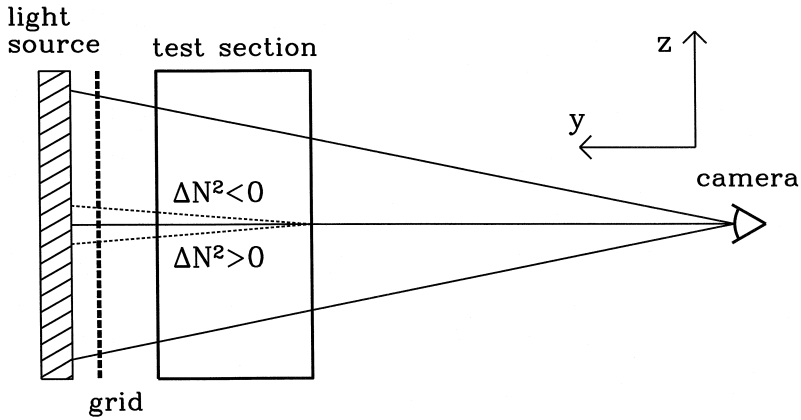

Fig. 2. Schematic showing the set-up used for synthetic schlieren. The three solid lines from the light source to the camera represent light rays which pass through a tank of salt-stratified water. The small dashed lines departing from the centre ray represents the deflected ray path taken if the density gradient (and hence the squared buoyancy frequency) changes due to internal gravity waves.

back-illuminated by a rack of fluorescent tubes, pass at angles close to the horizontal through a tank filled with salt stratified water. The deflected rays then enter a CCD camera, and the resulting signal is either recorded directly to tape or is digitally processed through a frame-grabber card and stored on hard-disk using ‘‘DigImage’’, an image processing software package (Dalziel, 1992). The digitised intensities are assigned integer values between 0 and 255. In these experiments, the illuminated image is a grid of horizontal black and white lines from which it is possible to determine changes in the vertical density gradient of the fluid. An image of a random pattern of dots may also be used, in which case it is possible to measure simultaneously the horizontal and vertical density gradients (Dalziel et al., 1999). The camera is placed as far from the tank as practical, typically about 350 cm away, so as to minimise the angle with which the light ray enters the camera. For these experiments, the angle is less than approximately 2°. An initial digitised image is recorded to calibrate the light source. During an experiment, departures from the initial intensities are recorded and used to visualise and measure the wave amplitudes.

Experiments are performed in a tank with test section 20 cm wide by 40 cm tall. The length of the test section is over 200 cm long so that end effects are negligible. Using a double bucket system, an approximately uniform stratification is established with $N^2 \simeq 1 \pm 0.1\ \mathrm{s}^{-2}$ over 35 cm depth. A circular cylinder of radius $R = 1.67$ cm is suspended with its centre approximately 25.7 cm above the bottom of the tank and is oriented so that its horizontal axis spans the width of the tank. The cylinder is constructed from a PVC tube with removable ends which allow it to be partially filled with water in order to reduce its effective weight when suspended underwater. The cylinder is supported by a thin metal rod attached to its centre.

The other end of the rod is attached 45 cm along a sinusoidally oscillating arm by a hinge, and the rod itself is confined to pass through a rigid guide so that the cylinder

undergoes approximately sinusoidal oscillations along a line. When oscillating vertically, the peak to peak displacement of the cylinder is 0.64 cm, approximately 20% of the cylinder diameter. The amplitude A is defined to be the maximum displacement of the cylinder from its equilibrium position. For a vertically oscillating cylinder, $A = 0.32$ cm, and for a cylinder that oscillates along an axis at an angle ϕ to the vertical, the amplitude is $A = 0.32(\cos\phi)$ cm. The flow about the cylinder is laminar for all oscillation frequencies and amplitudes examined. Time series constructed from images of the moving cylinder confirm that it moves sinusoidally; power spectra exhibit negligible amplitude outside a narrow range about the oscillation frequency.

The results of a typical experiment are shown in Fig. 3. Here, the cylinder oscillates vertically with frequency $\omega \simeq 0.35\ \mathrm{s}^{-1}$. Fig. 3a shows the digitised image taken by the camera before the cylinder begins oscillating. The image shows the end view of the cylinder, the suspending rod and the illuminated grid of horizontal lines behind the tank. Fig. 3b shows the image taken after the cylinder has completed four oscillations and is moving downward through its equilibrium position. Although Fig. 3a and b are similar, minute displacements of the lines near the cylinder are clearly visible. Indeed, although not visible to the naked eye, the lines far from the cylinder are displaced due to the wave field. The discrepancy between Fig. 3a and b is made apparent by determining the absolute value of the difference between the intensities of each pixel in the two

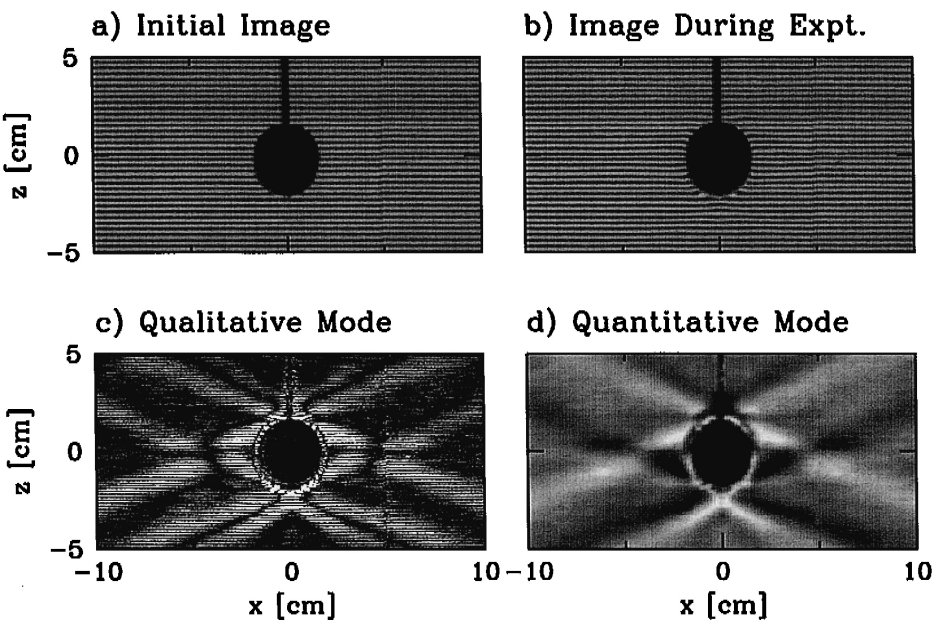

Fig. 3. Internal waves generated by a vertically oscillating cylinder visualised by synthetic schlieren. The side view of the cylinder and background grid lines is shown (a) before the cylinder starts moving and (b) after it has oscillated four times. Image (c) is produced by subtracting and scaling the intensities of the images shown in (a) and (b). In (d), the ΔN^2 field is shown as calculated from the images shown in (a) and (b). The values corresponding to the gray scale range from -0.15 (black) to $0.15\ \mathrm{s}^{-2}$ (white). See the text for more details.

diagrams. Fig. 3c is produced by performing this operation over the entire field and multiplying the result by a scaling factor of 20. The image shows the internal wave field consisting of four beams. The figure shows that the amplitude of the waves near the cylinder is largest along tangents to the cylinder parallel to the direction of the beam and is small along a line through the centre of each beam. The viscosity length-scale given by Eq. (3) is $l_v \simeq 10$ cm in this experiment, which is much larger than the cylinder diameter $2R \simeq 3.3$ cm. Thus, on the basis of Makarov et al. (1990), the beam near the cylinder is expected to be bimodal, a result consistent with experiments. The arithmetic operations used to determine this image may be performed in real time thus allowing continuous visualisation of the internal wave field during the course of an experiment.

Although qualitative information (e.g., the frequency and angle of the wave beams) may be derived from an image such as that in Fig. 3c, the image does not directly reveal any quantitative information about the amplitude of the waves. As shown in Section 4, however, it is possible to relate the intensity change of a pixel to the deflection of a light ray, and from this calculate the density gradient field. Fig. 3d shows the result of this calculation determined from the images in Fig. 3a and b. The figure shows the change in the squared buoyancy frequency field $\Delta N^2(x,z)$. The field is shown as a gray-scale for values ranging from -0.15 (black) to 0.15 s^{-2} (white). Inspection of this field shows, for example, that the density gradient changes by as much as 10% close to the cylinder. The details of how the ΔN^2 field is calculated are given below.

3.3. Quantitative measurement of internal wave amplitudes

Consider the path followed by a light ray passing from the camera through the tank to the image, as shown in Fig. 2. The (x,y,z) co-ordinate system is oriented with z vertical, y horizontal across the span of the tank toward the image, and x horizontal in the along-tank direction to the right facing the image. It is assumed that the variations of refractive index in the y-direction through the tank are negligible. This assumption is reasonable due to the geometry of the experimental set-up. The only spanwise variations that do, in fact, occur are within the boundary layers at the side walls of the tank. From boundary layer theory, the total thickness of the two layers is approximately 2 mm, or about 1% of the tank width. Although such research has not yet been performed in detail, it is worth noting that synthetic schlieren could also be used to visualise internal waves that are not spanwise uniform, such as those generated by an oscillating sphere. In this case, the deflected light ray would yield some measure of the average variation of n across the span of the tank. A detailed discussion of this circumstance is beyond the scope of the present paper.

In order to simplify this discussion for the oscillating cylinder, as well as assuming the refractive index is independent of y, it is assumed that the path of the light ray lies in the y–z plane. A more general treatment, including deflections in the x direction is given by Sutherland et al. (1999). If the ray passes through the tank with a small positive angle to the horizontal, then, as it propagates upward into less dense fluid the index of refraction is smaller, and the ray is refracted towards the horizontal. Specifically, the path taken by the ray satisfies Snell's Law,

$$n\cos\varphi = \text{constant}, \tag{10}$$

in which $n = n(z)$ is the index of refraction and $\varphi = \varphi(y, z)$ is the angle the ray makes with the horizontal. The angle is given in terms of the slope of the ray with the horizontal by

$$\frac{\mathrm{d}z}{\mathrm{d}y} = \tan\varphi. \tag{11}$$

Combining these gives a differential equation for z in terms of y. Explicitly, taking the y-derivative of Eq. (10) and using Eq. (11) it is found that

$$\frac{\partial\varphi}{\partial y} = \frac{n'(z)}{n(z)}. \tag{12}$$

Then, taking the y-derivative of Eq. (11) and using Eq. (12) and the fact that $|\varphi| < 2°$, the equations simplify to

$$\frac{\mathrm{d}^2 z}{\mathrm{d}y^2} = \frac{n'(z)}{n(z)}, \tag{13}$$

the solution of which describes the path taken by the light ray through the tank (Sutherland et al., 1999).

In the absence of strong mixing or layering, it is valid to assume that the refractive index varies linearly over the small depth traversed by the light ray (typically less than 1 cm) and that the refractive index varies linearly with density (Weast, 1981). Then, after some simplification of the solution to Eq. (13), the vertical displacement of the ray, z, is found as a function of the spanwise distance across the tank y:

$$z(y) \simeq y\tan\varphi_i - \frac{1}{2}\gamma N^2 y^2, \tag{14}$$

where φ_i is the angle to the horizontal of the ray entering the tank on the camera side, and

$$\gamma = \frac{1}{g}\frac{\rho_0}{n_0}\frac{\mathrm{d}n}{\mathrm{d}p} \simeq 1.878 \times 10^{-4}\,\mathrm{s}^2/\mathrm{cm}, \tag{15}$$

in which n_0 is a reference value of the index of refraction.

Eq. (14) shows that the effect of stable stratification is to bend a nearly horizontal light ray along a (concave downward) parabolic arc. Thus, a local increase in the density gradient in the tank acts to deflect a light ray downward, and the image behind the tank appears to shift upward. Because the angle of the ray leaving the tank changes, the farther the image is positioned behind the tank the greater its apparent vertical displacement.

Quantitative measurements of the density gradient field are obtained by relating it to the apparent displacement of horizontal grid lines in the image. By the repeated application of Snell's Law as the light ray passes from the grid to the camera, the change in the squared buoyancy frequency is found as a function of the apparent vertical displacement field Δz of the image:

$$\Delta N^2 \simeq -\Delta z \frac{1}{\gamma}\left[\frac{1}{2}L_{\mathrm{tank}}^2 + L_{\mathrm{tank}}L_{\mathrm{screen}}\frac{n_{\mathrm{water}}}{n_{\mathrm{air}}}\right]^{-1}, \tag{16}$$

in which n_{air} and n_{water} are the refractive indices of air and water, taken to be 1 and 1.333, respectively, $L_{\text{tank}} \simeq 20.0$ cm is the width of the tank, and $L_{\text{screen}} \simeq 34.2$ cm is the distance between the tank and the image. Here, the thickness of the tank walls is assumed to be negligibly small. Substituting these values in Eq. (16) gives $\Delta N^2 \simeq -0.2\Delta z$, in which the fields of $\Delta N^2(x,z)$ and $\Delta z(x,z)$ are measured in units of s^{-2} and cm, respectively.

The experiment is set up so that a pixel appears to shift vertically by no more than its height. Knowing the position and intensities of three vertically aligned pixels, the vertical displacement of the centre pixel is estimated by quadratic interpolation. Specifically, if during an experiment the intensity I' of a pixel changes from its initial value I_0, then, the apparent displacement is

$$\Delta z = (z_{-1} - z_0)\frac{(I' - I_0)(I' - I_1)}{(I_{-1} - I_0)(I_{-1} - I_1)} + (z_1 - z_0)\frac{(I' - I_0)(I' - I_{-1})}{(I_1 - I_0)(I_1 - I_{-1})}. \quad (17)$$

in which z_{-1}, z_0 and z_1 are the co-ordinates of the centres of the three pixels, and I_{-1}, I_0 and I_1 are the respective initial intensities. Note, if there is no intensity change of the middle pixel (that is, if $I' = I_0$), then, $\Delta z = 0$. Eq. (17) is solved only if $I_1 < I_0 < I_{-1}$ or $I_{-1} < I_0 < I_1$, and the intensity contrast across the three lines is sufficiently large: $|I_1 - I_{-1}| > \Delta I_{\text{min}}$, in which the threshold ΔI_{min} is set explicitly. Typically, $\Delta I_{\text{min}} = 10$.

Once Δz has been determined, Eq. (16) is applied to determine ΔN^2. Points for which Δz could not be calculated are determined by working out the weighted average of the neighbouring calculated values. A Gaussian weighting factor is used, its magnitude decreasing with increasing distance from the center pixel being determined. The image is then filtered and averaged in order to reduce noise, as described below.

Even though a single pixel typically spans a vertical distance of 0.05 cm in the experiments reported here, it is estimated that apparent displacements corresponding to approximately $1/25$ of the pixel spacing (0.002 cm) can be visualised. For typical experiments, the noise filtered Δz field provides quantitative measurements accurate to ± 0.01 cm. As a result, using Eq. (16) and the experimental data that follows it, ΔN^2 can be detected in theory for values as small as $0.002\ \text{s}^{-2}$. However, the actual error in the measurement of ΔN^2 is significantly greater due to noise, which is dominated by rapid variations in the temperature of the laboratory, degradation of the image quality through storage on video tape, and changes in the light source intensity.

In order to reduce noise effectively, vertical time series are constructed from video images. Pixel scale noise is reduced by replacing each pixel value with the spatio-temporal average of the surrounding 5 by 5 square pixel region. The result is then put through a low pass filter in the time domain to reduce contamination of the signal due to temperature variations, and the mean value in time is subtracted to reduce the effect of gradually increasing temperatures and light intensities. This is done for a range of vertical time series determined along a sequence of horizontal positions. After filtering, the two-dimensional spatial field of view is reconstituted at particular times.

Before filtering, the standard deviation in values of ΔN^2, determined from calibration test images is approximately $0.05\ \text{s}^{-2}$. After filtering the resulting measurements have an associated error of $0.01\ \text{s}^{-2}$. This estimate is determined by noting that the

dominant noise signal at a particular pixel is reduced at the first step by averaging over 25 surrounding pixels.

In some circumstances, it is convenient to estimate the time derivative of the N^2 field, N_t^2. Effectively, N_t^2 is a measure of the rate of stretching and compression of vertical density gradients. It is calculated from a finite difference approximation to the time derivative by determining Δz at successive times spaced at intervals much less than the period of the wave-motion. Sutherland et al. (1999) have demonstrated that the basic state fields of perturbation density and horizontal and vertical velocity may be estimated from the ΔN^2 and N_t^2 fields. In order to assist in developing an intuition for these relationships, here, we present them for the special case of plane periodic internal waves with frequency ω and wavenumber vector (k_x, k_z):

$$u = -\iota/k_x\left(N_t^2/N^2\right); \quad \omega = \iota/k_z\left(N_t^2/N^2\right);$$
$$\rho = \rho_0(\iota/gk_z)\Delta N^2; \quad \text{and} \quad \zeta = \iota/k_z\left(\Delta N^2/N^2\right). \tag{18}$$

In the last of these relationships, ζ is the vertical displacement field associated with the internal waves. Note that each basic state field is phase-shifted by $\pm\pi/2$ from the ΔN^2 and N_t^2 fields.

The relationships given by Eq. (18) may be used as a double check on the experimental results. For example, by tracking the horizontal displacements of a vertical line of dye (e.g., from a dropped potassium permanganate crystal), an independent measure of the horizontal velocity field can be determined and compared with u, determined from Eq. (18). An analysis of this kind was performed by Sutherland and Linden (1998).

4. Qualitative results

Using the synthetic schlieren technique, we have performed a range of experiments to study the structure and amplitude of internal waves generated by a cylinder oscillating at an angle ϕ to the vertical. In each experiment, the cylinder is positioned near $z = 25$ cm above the bottom of the tank. Before the experiments are performed, a conductivity probe is traversed downward through the fluid to measure the density profile. The probe moves downward at 4 cm/s taking samples at a rate of 100 Hz. The density profile for the experiments reported here is shown in Fig. 4a. Fig. 4b shows the profile of the squared buoyancy frequency calculated from the density profile. The figure shows that $N^2 \simeq 1\ \text{s}^{-2}$ at the depth of the centre of the cylinder, and is moderately larger $(1 < N^2 < 1.2\ \text{s}^{-2})$ below the cylinder.

Fig. 5 shows the wave-beams emanating from a cylinder oscillating at angles (a) $\phi = 0°$, (b) 15.8°, (c) 22.6° and (d) 36.8° from the vertical. The angle of oscillation increases counter-clockwise from the vertical for larger values of ϕ. In each experiment, the cylinder oscillates at a frequency $\omega \simeq 0.53\ \text{s}^{-1}$, thus, producing four wave-beams each of which is expected to emanate from the cylinder at an angle $\Theta \simeq 58°$ to the vertical. In each diagram, the wave field is shown over a region extending from $-8 < x < 8$ cm to $-10 < z < 2$ cm. The cylinder, which is centred at the origin, is superimposed in white. Note that the camera is centred approximately 4 cm below the

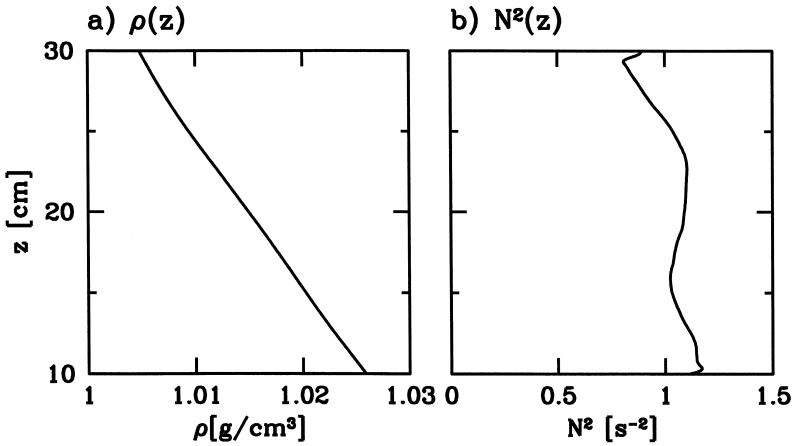

Fig. 4. Initial experimentally measured vertical profiles of (a) density and (b) the squared buoyancy frequency.

centre of the cylinder: the image is recorded of both the end and underside of the cylinder and, thus, the vertical extent of the cylinder appears larger than its actual radius. The contours show values of the ΔN^2 field associated with the internal waves after the cylinder has completed at least four oscillations and it is moving downward through its equilibrium position. The contours range from -0.12 to 0.12 s^{-2}, as illustrated. The most obvious effect of changing the angle of oscillation is to change the relative phase of the downward right and left propagating internal wave-beams. When $\phi = 0.0$, the two beams are symmetric about a vertical line through the centre of the cylinder. The upward and downward propagating beams to the right of the cylinder are approximately anti-symmetric about a horizontal line through the centre of the cylinder. The same is true of the upward and downward propagating beams to the left of the cylinder.

When the cylinder oscillates at an angle to the vertical, the symmetry is broken between the downward right and left propagating wave-beams. The relative phase of the beams changes so that, for example, the amplitude of the ΔN^2 field on the lower flank of the left propagating wave-beam is smaller compared with the right propagating wave-beam as ϕ increases. The change in phase with increasing ϕ of the upward and downward propagating waves is also apparent to the right and left of the cylinder. When $\phi = 0°$, there is a positive and negative peak in the ΔN^2 field approximately 0.5 cm above and below the line $z = 0$, respectively. When $\phi = 36.8°$, there is a negative peak centred just below the line $z = 0$ to the right of the cylinder and a positive peak centred just above the line $z = 0$ to the left of the cylinder.

To demonstrate the phase change in more detail, Fig. 6 shows four time series constructed from a cross-section along a vertical line directly below the cylinder centre along $x = 0$. The experiments from which each diagram is determined correspond with those shown in Fig. 5 with (a) $\phi = 0°$, (b) 15.8°, (c) 22.6° and (d) 36.8°. The cylinder oscillates at a frequency $\omega \simeq 0.72$ s^{-1} in each case. The time evolution of the waves is shown over 20 s from $-6 \leq z \leq -1$ cm, the time series ending when the cylinder moves downward through its equilibrium position. The contours show the time rate of

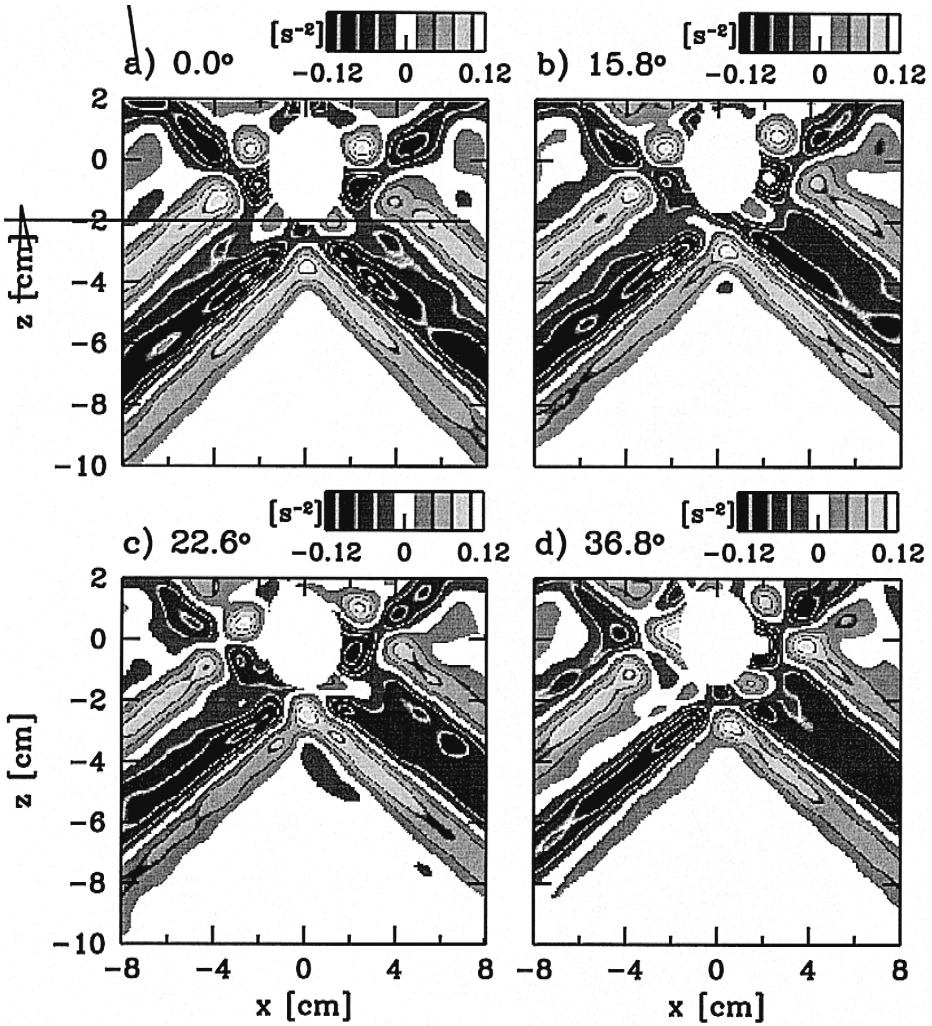

Fig. 5. ΔN^2 field about a cylinder oscillating about an angle ϕ to the vertical with (a) $\phi = 0.0°$, (b) 15.8°, (c) 22.6°, and (d) 36.8°. In each case, the cylinder oscillates at frequency 0.53 s^{-1}, which generates internal waves that propagate at angles $\Theta \simeq 58°$ to the vertical.

change of the squared buoyancy frequency field N_t^2 with values ranging from -0.25 to 0.25 s^{-3}, as illustrated. In each diagram, the lines of constant phase propagate upward with increasing time. This behaviour is expected because internal waves with downward group velocity have upward phase speed.

The pattern of waves illustrates the effect of changing ϕ upon the relative phases of the right and left propagating wave-beams. Consider the time and depth at which the maximum and minimum value of N_t^2 occurs. Although it is not clear precisely where the maximum occurs in the case with $\phi = 0°$ (Fig. 6a), both the positive and negative peaks occur at depths between $z = -4$ and -3 cm. For successively larger values of ϕ,

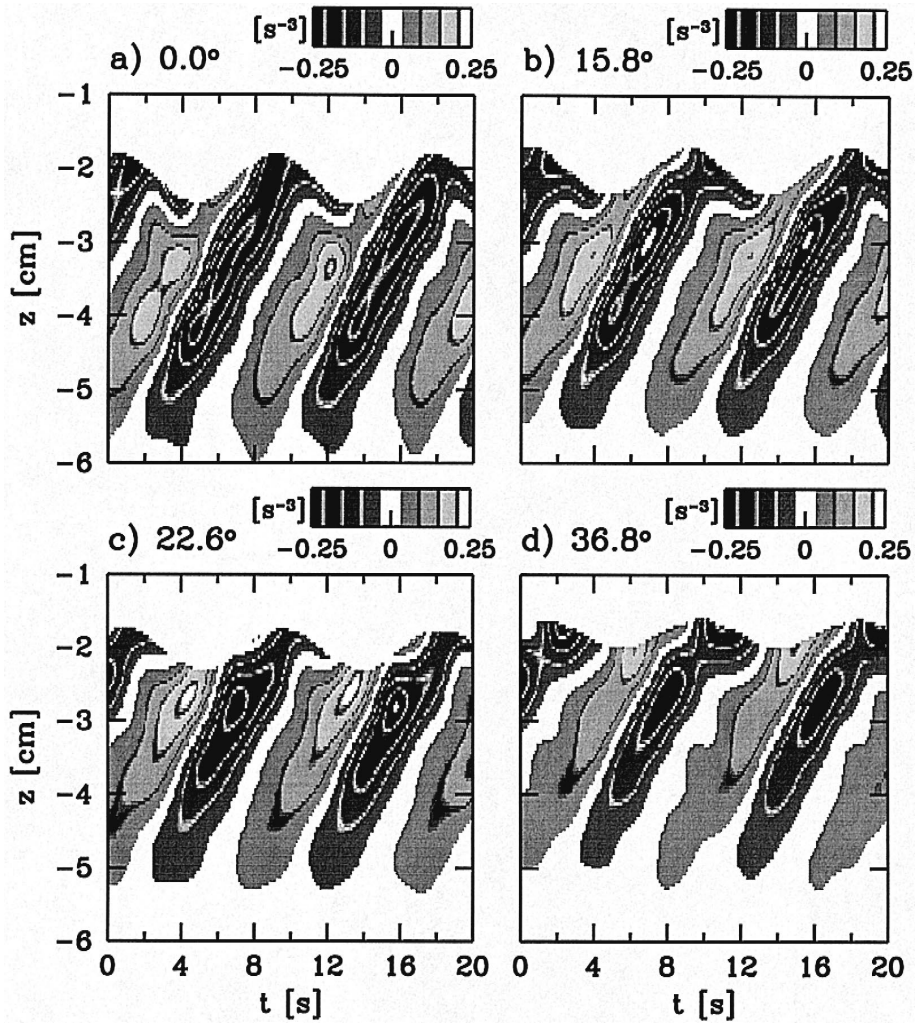

Fig. 6. Time series of a vertical cross-section taken directly beneath the cylinder at $x = 0$ for the cylinder oscillating with frequency 0.72 s^{-1} about an angle ϕ to the vertical with (a) $\phi = 0.0°$, (b) 15.8°, (c) 22.6° and (d) 36.8°.

the depth and phase of the cylinder oscillation for which the negative peak value of N_t^2 occurs is approximately the same: the peak occurs near $z = -3$ cm at a time when the cylinder moves upward through its equilibrium position. However, the positive peak value of N_t^2 occurs at a time closer in phase to the negative peak and it occurs at shallower depths ($z > -3$ cm). In particular, when $\phi = 36.8°$ (Fig. 6d), the peak is situated near the base of cylinder at about $z = -2$ cm and occurs shortly after the cylinder begins to move upward from its deepest displacement. Thus, as the cylinder oscillates at angles further from the vertical, the interference between the left and right

wave-beams is more destructive. Indeed, linear theory predicts that if the cylinder oscillates horizontally, the N_t^2 field of the two beams should destructively interfere along $x = 0$.

5. Comparison with theory

A range of experiments have been performed in which we compare observations and theory for internal waves generated by a cylinder oscillating with different amplitudes and a range of angles to the vertical. Future work will examine how the wave field depends upon the shape of the cylinder itself.

A detailed study of the dependence of the internal wave field amplitude upon the amplitude of a vertically oscillating cylinder is given in Sutherland et al. (1999). In this paper, we review the comparison of experiments with the theory of Hurley and Keady (1997) for the structure of the wave field produced by a cylinder oscillating vertically at four different frequencies. We then examine how the structure of the wave field depends upon the angle of oscillation with the vertical. Future work will examine how the wave field depends upon the shape of the cylinder itself.

5.1. Cylinder oscillating at different frequencies

Fig. 7 shows the downward and right propagating internal wave beam generated from a cylinder that oscillates vertically at frequencies (a) $\omega = 0.15$ s^{-1}, (b) 0.35 s^{-1}, (c) 0.53 s^{-1} and (d) 0.72 s^{-1}. Because linear theory predicts that density perturbations scale with the cylinder amplitude it is convenient to show contours of the ΔN^2 field normalised by the cylinder amplitude $A = 0.32$ cm. The contours range from -0.5 to 0.5 s^{-2} cm^{-1}. In each case, the fields are shown as the cylinder moves downward through its equilibrium position. The waves are shown in a frame of reference rotated anti-clockwise by an angle $90° - \Theta_r$, with Θ_r determined so that in each case the lines of constant phase of the right and downward propagating beams between $10 \le r \le 15$ cm are, on average, horizontal. In (a) $\Theta_r = 78.9°$, (b) 66.1°, (c) 54.2° and (d) 39.4°. In this frame, the horizontal (r) axis is the along-beam direction and the vertical (σ) axis is the across-beam direction oriented so that $\sigma > 0$ corresponds with the upper flank of the wave beam. (Note, this orientation for σ is opposite to that used by Hurley and Keady (1997).)

The buoyancy frequency of the fluid is $N \simeq 1.02 \pm 0.04$ s^{-1}, determined from the mean and standard deviation of the experimentally measured $N(z)$ profile for $10 \le z \le 30$ cm. From linear theory, the corresponding angle of propagation of the beams with the vertical is expected to be (a) $\Theta \simeq 81.5 \pm 0.3°$, (b) $69.9 \pm 0.8°$, (c) $58.7 \pm 1.5°$, and (d) $45.1 \pm 2.4°$, respectively, for the four diagrams in Fig. 7. Although $\Theta_r \simeq \Theta$ is expected, we find that Θ_r is consistently smaller than Θ: in (a) $\Delta\Theta \simeq 2.6°$, (b) 3.8°, (c) 4.5° and (d) 5.7°, in which $\Delta\Theta = \Theta - \Theta_r$. The reason for this discrepancy is unclear. Parallax, while playing a small role, does not account for the observed apparent deflection of the beam. It is possible that the deflection occurs because the width of the beam is comparable with the scale of the background buoyancy frequency variations (Sutherland and Linden, 1999), or that it is an artifact of the broadening beam as it attenuates.

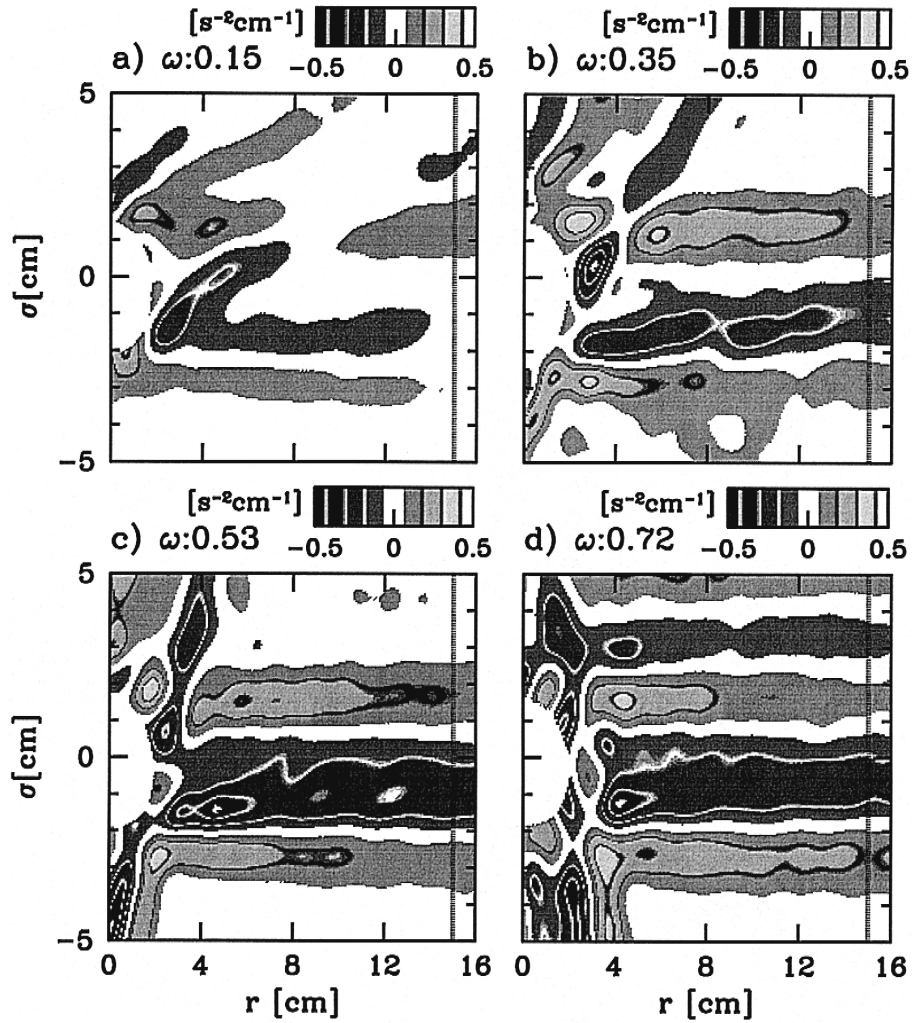

Fig. 7. Normalised $\Delta N^2/A$ field for a vertically oscillating cylinder with amplitude A, oscillating at frequencies (a) $\omega = 0.15$ s^{-1}, (b) 0.35 s^{-1}, (c) 0.53 s^{-1} and (d) 0.72 s^{-1}. The background buoyancy frequency is $N \simeq 1.02 \pm 0.04$ s^{-1}. The right and downward propagating beam of waves is shown in a (r, σ) co-ordinate system. The vertical dashed line at $r = 9R$ indicates where a cross-section is taken for comparison with theory.

In experiments performed with the cylinder oscillating at frequency $\omega \simeq 0.72$ s^{-1}, upward propagating waves reflect from the water surface and significantly interfere with the wave beams that propagate downward from the cylinder. The interference between the reflected and downward propagating wave beams can be seen in Fig. 7d. Here, the positive and negative peaks above $\sigma \simeq 2$ cm are associated with the reflected waves. The lower flank of the reflected beam interferes with the upper flank of the downward propagating beam originating from the cylinder at about $\sigma \simeq 2$ cm, but the interference

is negligible on the lower flank of the beam ($\sigma < 0$ cm). In general, the diagrams show that the amplitude of the waves is larger if the cylinder oscillates with larger frequency.

Fig. 8 shows the amplitude of the observed (dashed line) and theoretically predicted (solid line) wave field determined from the four experiments shown in Fig. 7. The plots of $\Delta N^2/A$ are shown along cross-sections perpendicular to the beam, centred at a distance $9R$ from the centre of the cylinder as indicated by the vertical dashed line in each diagram of Fig. 7. The distance is chosen to be sufficiently far along the wave beam from the cylinder that the superposition of the upward propagating wave beam upon it can be neglected in the case with $\omega = 0.35\ \mathrm{s}^{-1}$. The structure of the wave beam at a range of distances from the cylinder is examined by Sutherland et al. (1999).

In each diagram, the range of experimental error is indicated in the top left-hand corner. From the estimates given at the end of Section 3.3, the error in the amplitude is

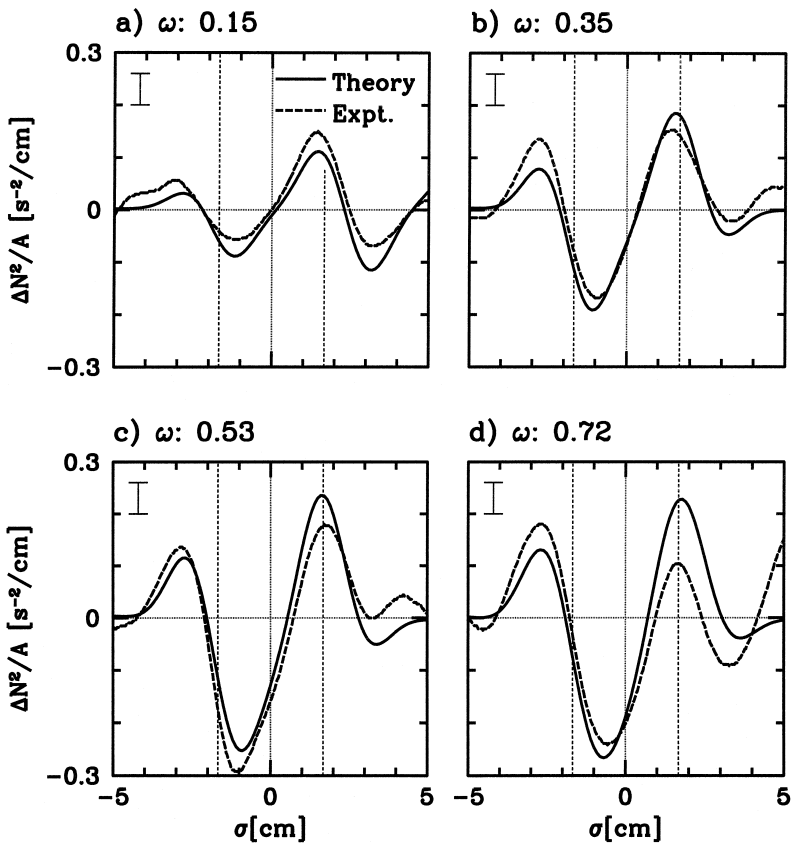

Fig. 8. Comparison between theory (solid line) and experiment (dashed line) of the normalised $\Delta N^2/A$ field along a cross-section perpendicular to the beam taken nine cylinder radii from the source. The cross-sections are taken from the corresponding diagrams in Fig. 7. The vertical dashed lines in each plot indicate the radius of the cylinder. The ranges shown in the top left corner of each plot indicate the experimental error.

given by $\pm 0.01/A \simeq \pm 0.03$. The error in time is estimated by assuming the desired phase of the waves can be determined within 0.5 s of the actual time at which they occur.

In each of the four cases shown, the across-beam structure is well reproduced by the theoretical prediction given by Eq. (9). In the case with $\omega = 0.15$ s^{-1}, the theoretical structure of the upward propagating wave beam is superimposed, as it is necessary in this case to account for interference of the upper and lower beams at $r = 9R$. In Fig. 8a–c, the discrepancies between theory and experiment are within experimental error. In Fig. 8d, the differences between experiment and theory for $\sigma > 1$ cm may be attributed to the interference of the surface reflected wave beam with the upper flank of the downward propagating wave beam, as discussed above.

Although the theoretically predicted amplitude is within errors, in general, some consistent discrepancies exist. We find that in each case the width of the beam is underpredicted by theory by approximately $10 \pm 6\%$. This discrepancy is examined more closely by Sutherland et al. (1999), who argue that it occurs because linear theory neglects the viscous boundary layers surrounding the cylinder, that effectively act to increase the size of the source. This is not to say that a theoretical solution, rescaled to account for the effective increase in size of the source, would be sufficient to predict accurately the experimental results. For example, whereas the width of the beam is consistently underpredicted, as shown below, the amplitude of the waves is apparently both over- and underpredicted, depending on the wave frequency.

A comparison between the experimental and theoretical profiles shows that theory overpredicts the peak positive amplitude observed on the upper flank of the beam, except in the case with $\omega \simeq 0.15$ s^{-1}. This discrepancy is believed to be an artifact of errors in the time (± 0.5 s) at which the images are analysed from video images of the experiment. As a result, the phase of the waves may differ from theory by as much as 6%.

However, what cannot be attributed to such an artifact is that theory overpredicts the peak-to-peak amplitude of the waves by approximately 5% for the case with the cylinder oscillating with frequency $\omega \simeq 0.53$ s^{-1} (Fig. 8c). For the case with $\omega \simeq 0.72$ s^{-1} (Fig. 8d), the theoretically predicted peak amplitude on the upper flank of the beam is more than twice as large as the experimentally determined amplitude. This occurs because waves that have reflected downward from the surface of the tank interfere with the downward propagating beam emanating from the cylinder. Nonetheless, by analysis of a range of experiments, not reported here, we find in general that theory overpredicts the amplitude of large frequency waves. Although it is possible that this discrepancy may be an artifact of the way in which the experimental data is noise-filtered (the procedure acting to smooth the observed profiles), it seems likely that the amplitude of the waves would be smaller in experiments in part because a fraction of the energy associated with them is dissipated in the boundary layer surrounding the cylinder. A more detailed study of the boundary layer dynamics is necessary to determine how.

In general, though not clear from Fig. 8a, we also find that theory moderately underpredicts the amplitude of small frequency waves. Sutherland et al. (1999) argue that this may be the result of wave-wave interactions that occur over the relatively large region where the upward and downward propagating wave beams overlap.

5.2. Cylinder oscillating at an angle with the vertical

Fig. 9 shows the structure of the downward and right propagating wave beam generated by a cylinder oscillating at angles (a) $\phi = 0.0°$, (b) 15.8°, (c) 22.6° and (d) 36.8° to the vertical. The fields are shown as the cylinder moves downward through its equilibrium position. In each case, the cylinder oscillates at frequency $\omega \simeq 0.35\ \mathrm{s}^{-1}$, and the amplitude of oscillation is given by $A \simeq 0.32(\cos\phi)$ cm. As in Fig. 7, the diagrams

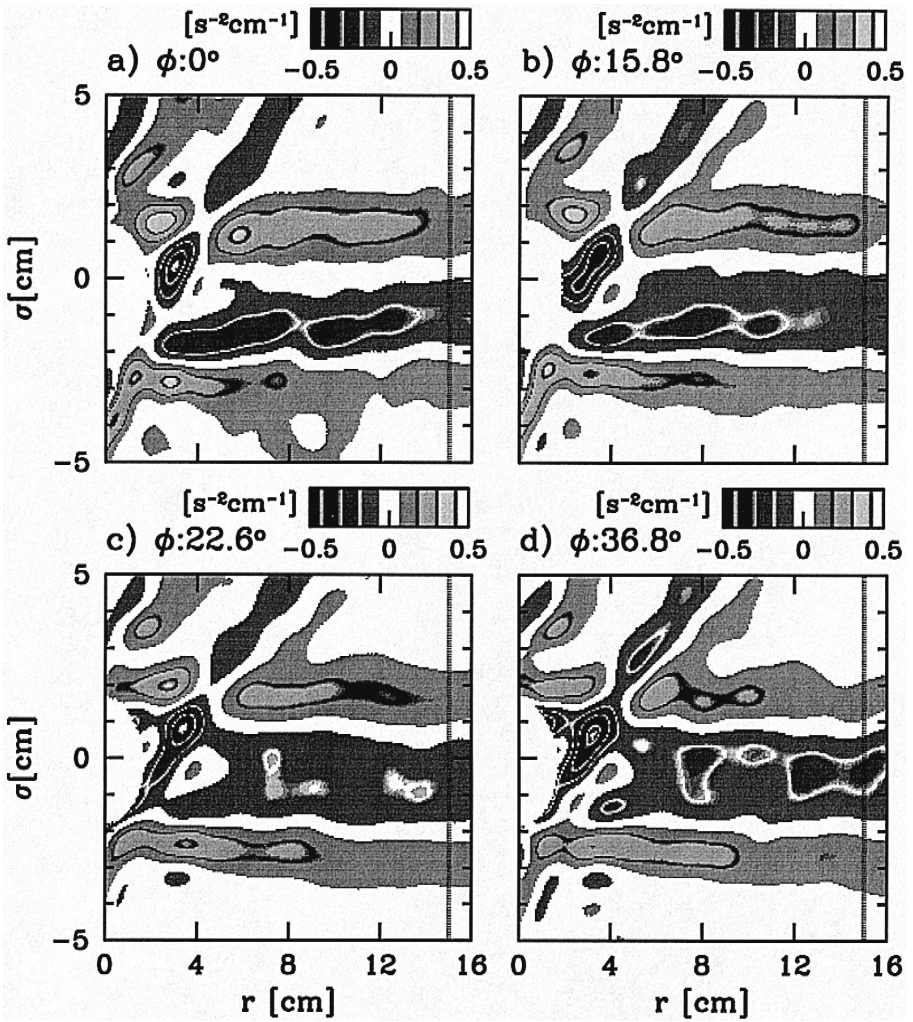

Fig. 9. Normalised $\Delta N^2/A$ field for a cylinder oscillating with amplitude A about an angle ϕ to the vertical with (a) $\phi = 0°$, (b) 15.8°, (c) 22.6° and (d) 36.8°. In each case the cylinder oscillates at frequency $\omega \simeq 0.35\ \mathrm{s}^{-1}$ and the background buoyancy frequency is $N \simeq 1.02 \pm 0.04\ \mathrm{s}^{-1}$. The waves are shown in a (r,σ) co-ordinate system, rotated by counter-clockwise about an angle Θ_r so that the downward and right propagating wave beam is approximately horizontal. In (a), $\Theta_r = 66.1°$, (b) 68.4°, (c) 70.1° and (d) 70.0°.

show contours of $\Delta N^2/A$ in a (r,σ) co-ordinate system rotated counter-clockwise by an angle $90° - \Theta_r$, so that the beams in this system are approximately horizontal. The contours range from -0.50 to 0.50 s^{-2} cm^{-1}. From linear theory, we expect the beams to propagate at an angle $\Theta \simeq 70.4 \pm 1.0°$ from the vertical. However, we find the angle of propagation to the vertical is consistently less by an amount (a) $\Delta\Theta = 4.3°$, (b) 2.0°, (c) 0.3° and (d) 0.4°.

The experimental results are compared with theory in Fig. 10. along a span-wise cross-section taken at $r = 9R$, as indicated by the dashed line on each diagram of Fig. 9. The normalised $\Delta N^2/A$ fields determined theoretically (solid line) and experimentally (dashed line) are shown. The agreement between theory and experiment is generally good in each case. However, the predicted width of the beam is consistently smaller than the observed width. Based on the distance between the two positive peaks, we find that the theory underpredicts the experimentally determined width by approximately $7 \pm 4\%$.

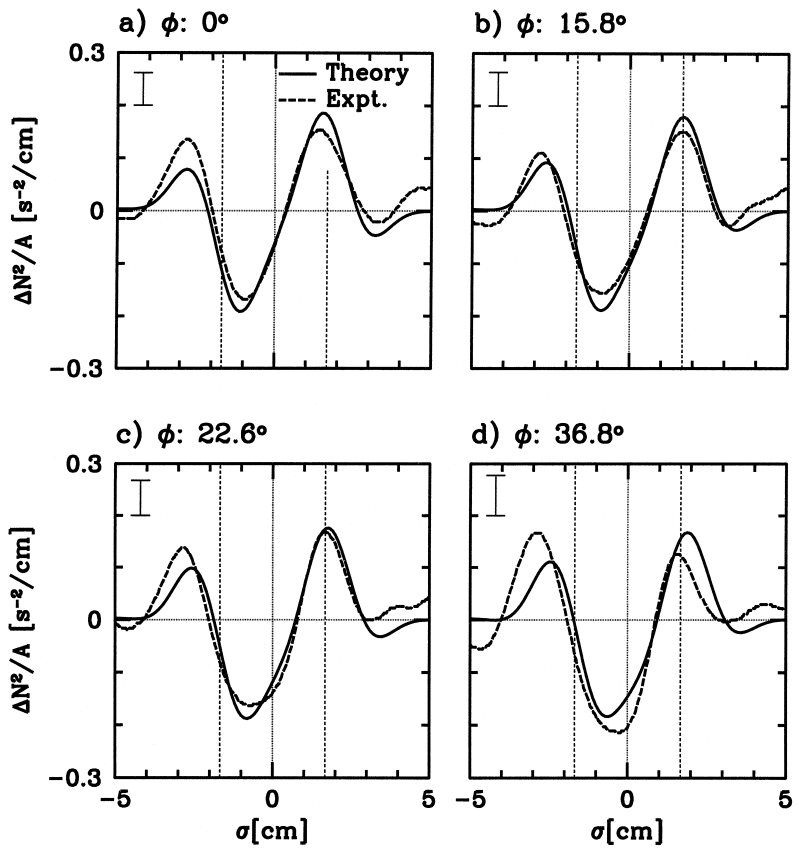

Fig. 10. Comparison between theory (solid line) and experiment (dashed line) of the normalised $\Delta N^2/A$ field along a cross-section perpendicular to the beam taken nine cylinder radii from the source. The cross-sections are taken from the corresponding diagrams in Fig. 9. The vertical dashed lines in each plot indicate the radius of the cylinder. The ranges shown in the top left corner of each plot indicate the experimental error.

In addition, we find that theory underpredicts the peak positive amplitude of the waves on the lower and upper flank of the beam in all four cases. We attribute this discrepancy in part to errors in the time at which the analysed image is taken from video, as discussed above. In all four experiments, the theoretically determined peak-to-peak amplitude is moderately larger than that observed in experiments.

6. Conclusions

We have described a new ''synthetic schlieren'' technique for visualising and quantitatively measuring the amplitude of nominally two-dimensional internal waves. The technique is more robust than previously existing visualisation techniques in that it is relatively inexpensive to set up, it allows a wider field of view, and provides non-intrusive measurements of the amplitude of a quasi-two-dimensional wave field continuously in time. Furthermore, the technique is highly sensitive. In the experiments reported here, for example, fluid parcels displaced vertically by distances as small as 0.01 cm can be detected, and density gradient changes as small as 1% of the ambient density gradient can be measured.

Using this technique, we have performed experiments with a cylinder oscillating at a range of frequencies along an axis inclined to the vertical. Comparing the results with the theoretical predictions of Hurley and Keady (1997), we find generally good agreement. The difference between the theoretical and experimentally measured amplitudes is well within experimental error across the width of the beams measured nine radii from the source, except in cases where the beams are contaminated by surface-reflecting wave beams. When comparing theory with a range of experiments, however, consistent though small discrepancies are found to exist.

We find that the width of the wave-beam is underpredicted by theory by as much as 10%. We believe this is due to the viscous boundary layer around the cylinder not being included in current theories for the structure of these waves. Viscous boundary layers act effectively to increase the size of the source. Indeed, order of magnitude estimates of the boundary layer size by Sutherland et al. (1999) agree with the observed difference in width between theory and experiment.

Both theory and experiment show that the amplitude of the waves increases as a function of frequency, but is a weak function of the angle of oscillation of the source. However, theory moderately overpredicts the peak to peak amplitude of large frequency waves. This is attributed in part to viscous dissipation in the boundary layer surrounding the cylinder, which is not accounted for in theory. It is also found that, in general, theory underpredicts the peak-to-peak amplitude of low frequency waves. The reason for this is unclear at present but may result from changes to the structure of the wave beam due to weakly non-linear interactions between the upward and downward propagating waves, which overlap over a relatively large region when forced at low frequency. In ongoing research, such finite amplitude effects are being examined both experimentally and numerically for vertically oscillating elliptical cylinders.

To understand the effects of the boundary layer in more detail, a variation of the synthetic schlieren technique is presently being used in which, rather than measuring the

displacement of horizontal lines, the displacement of a random array of dots is tracked (Dalziel et al., 1999). With this set up, it will be possible to improve the resolution of measurements of the fluid motion in the boundary layer.

Acknowledgements

This work has been supported in part by NERC under grant number GR3/09399.

References

Appleby, J.C., Crighton, D.G., 1986. Non-Boussinesq effects in the diffraction of internal waves from an oscillating cylinder. Q. J. Mech. Appl. Math. 39, 209–231.

Appleby, J.C., Crighton, D.G., 1987. Internal gravity waves generated by oscillations of a sphere. J. Fluid Mech. 183, 439–450.

Brandt, P.B., Alpers, W., Backhaus, J.O., 1996. Study of the generation and propagation of internal waves in the Strait of Gibraltar using a numerical model and synthetic aperture radar images of the European ERS 1 satellite. J. Geophys. Res. 101 (C6), 14237–14252.

Dalziel, S.B., 1992. Decay of rotating turbulence: some particle tracking experiments. Appl. Sci. Res. 49, 217–244.

Dalziel, S.B., Hughes, G.O., Sutherland, B.R., 1999. Whole-field density measurements by 'synthetic schlieren'. Experiments in Fluids, (in press).

Gill, A.E., 1982. Atmosphere–Ocean Dynamics. Academic Press, San Diego.

Hurley, D.G., 1997. The generation of internal waves by vibrating elliptic cylinders: Part 1. Inviscid solution. J. Fluid Mech. 351, 105–118.

Hurley, D.G., Keady, G., 1997. The generation of internal waves by vibrating elliptic cylinders: Part 2. Approximate viscous solution. J. Fluid Mech. 351, 119–138.

Huthnance, J.M., 1989. Internal tides and waves near the continental shelf edge. Geophys. Astrophys. Fluid Dyn. 48, 81–106.

Kistovich, A.V., Neklyudov, V.I., Chashechkin, Y.D., 1990. Non-linear two-dimensional internal waves generated by a periodically moving source in an exponentially stratified fluid. Izv. Atmos. Oceanic Phys. 26, 771–776.

Konyaev, K.V., Sabinin, K.D., Serebryany, A.N., 1995. Large-amplitude internal waves at the Mascarene Ridge in the Indian Ocean. Deep-Sea Res. I 42, 2075–2091.

Lighthill, M.J., 1978. Waves in Fluids. Cambridge Univ. Press, Cambridge, England.

Lilly, D.K., 1971. Observations of mountain-induced turbulence. J. Geophys. Res. 76 (27), 6585–6588.

Long, R.R., 1955. Some aspects of the flow of stratified fluids: III. Continuous density gradients. Tellus 7, 341–517.

Makarov, S.A., Neklyudov, V.I., Chashechkin, Y.D., 1990. Spatial structure of two-dimensional and monochromatic internal-wave beams in an exponentially stratified liquid. Izv. Atmos. Oceanic Phys. 26, 548–554.

Mowbray, D.E., Rarity, B.S.H., 1967. A theoretical and experimental investigation of the phase configuration of internal waves of small amplitude in a density stratified liquid. J. Fluid Mech. 28, 1–16.

Nastrom, G.D., Fritts, D.C., 1992. Sources of mesoscale variability of gravity waves: Part I. Topographic excitation. J. Atmos. Sci. 49, 101–110.

Peters, F., 1985. Schlieren interferometry applied to a gravity wave in a density-stratified fluid. Exp. Fluids 3, 261–269.

Press, W.H., Flannery, B.P., Teukolsky, S.A., Vetterling, W.T., 1993. Numerical Recipes: The Art of Scientific Computing, 2nd edn. Cambridge Univ. Press, New York.

Sakai, S., 1990. Visualisation of internal gravity waves by Moiré method. Kashika-Joho 10, 65–68.

Sutherland, B.R., Linden, P.F., 1998. Internal wave generation by flow over a thin barrier. J. Fluid Mech. 377, 223–252.

Sutherland, B.R., Linden, P.F., 1999. An experimental/numerical study of internal wave transmission across an evanescent level. In: Davies, P.A. (Ed.), Proceedings of the Fifth IMA Conference on Stratified Flows. Oxford Univ. Press, 251–261.

Sutherland, B.R., Dalziel, S.B., Hughes, G.O., Linden, P.F., 1999. Visualisation and measurement of internal waves by ''synthetic schlieren'': Part 1. Vertically oscillating cylinder. J. Fluid Mech. 390, 93–126.

Thomas, N.H., Stevenson, T.N., 1972. A similarity solution for viscous internal waves. J. Fluid Mech. 54, 495–506.

Toepler, A., 1864. Beobachtungen nach Einer neuen Optischen Methode. Max Cohen u. Sohn, Bonn.

Voisin, B., 1991. Internal wave generation in uniformly stratified fluids: Part 1. Green's function and point sources. J. Fluid Mech. 231, 439–480.

Weast, R.C., 1981. Handbook of Chemistry and Physics, 62nd edn. CRC Press.

Wunsch, C., 1975. Deep ocean internal waves: what do we really know? J. Geophys. Res. 80 (3), 339–343.

Wurtele, M.G., Sharman, R.D., Datta, A., 1996. Atmospheric lee waves. Annu. Rev. Fluid Mech. 28, 429–476.